Publishing Excellence Inspiring Progress
ARISTON PUBLICATIONS
Science of Alloys and Glasses
ISSN: 3143-0732 https://aristonpubs.com/journal/science-of-alloys-and-glasses https://doi.org/10.69626/sag.2025.0004

RESEARCH ARTICLE

Effect of Rare Earth Dopants on the Radiation Shielding Properties of Basic Oxide Glasses for High Energy Photon Applications

Badriah Sultan[1,*], Mohammed S. Alqahtani [2,3,4], Awad Almarhaby [5], Khalid I. Hussein [2,3,6], Nehal Elkhoshkhany [7,8], Ali M. Alshehri [1], Manuela Reben [9], Fawaz Alqahtani [10], El Sayed Yousef [1,3]

ABSTRACT: This study experimentally investigates the radiation shielding performance of novel tellurite-based glass systems doped with rare earth oxides. Glasses with composition $45TeO_2–25B_2O_3–20Bi_2O_3–7TiO_2–3RE$ (where RE = La_2O_3, Ce_2O_3, Sm_2O_3, Er_2O_3, and Yb_2O_3) were synthesized and characterized. The attenuation properties were evaluated using gamma-ray spectroscopy across multiple energy points (59.5 keV to 1330 keV) from Am-241, Cs-137, and Co-60 radioisotopes. Key radiation shielding parameters, including linear and mass attenuation coefficients, half-value layer, tenth-value layer, mean free path, effective atomic number, and fast neutron removal cross-section, were derived experimentally and further analyzed using the Phy-X/PSD software for a comprehensive energy range (0.015–15 MeV). Results demonstrate that all fabricated glasses exhibit substantial photon attenuation, with performance positively correlated with density. The Yb-doped glass (BBTTYb) displayed the highest density (6.31 g/cm³) and superior shielding characteristics, including the lowest half-value layer and mean free path across most energies. Enhanced attenuation is attributed to the increased effective atomic number and electron density provided by the heavy rare earth incorporation. These findings confirm that rare earth doping, particularly with Yb_2O_3, significantly improves the gamma-ray shielding capacity of tellurite glasses. The developed materials show strong potential for use in medical, industrial, and research facilities where effective radiation protection is required across a broad energy spectrum.

Keywords: Radiation shielding, Tellurite glass, Rare-earth doping, Gamma-ray attenuation, Protective materials

Received: 15 September 2024; Revised: 29 October 2024; Accepted: 03 December 2024; Published Online: 13 January 2025

[1] Physics Department, Faculty of Science, King Khalid University, Postcode- 9004, Zip code-61413, Abha, Saudi Arabia
[2] Department of Radiological Sciences, College of Applied Medical Sciences, King Khalid University, Abha-61421, Saudi Arabia
[3] Research Center for Advanced Materials Science (RCAMS), King Khalid University, Postcode- 9004, Zip code- 61413, Abha, Saudi Arabia
[4] BioImaging Unit, Space Research Centre, Department of Physics and Astronomy, University of Leicester, Leicester LE1 7RH, United Kingdom
[5] Medical Physics Department, King Fahd General Hospital, Ministry of Health, Al Andalus, Jeddah-23325, Jeddah.
[6] Department of Medical Physics and Instrumentation, National Cancer Institute, University of Gezira, Wad Medani-2667, Sudan.
[7] Physics Department, College of Arts and Sciences at Tabrjal, Jouf University, Sakaka-72388, Saudi Arabia
[8] Department of Material Science, Institute of Graduate Studies and Research, Alexandria University, 163 Horreya Avenue, Shatby, Alexandria 21526, Egypt
[9] Faculty of Materials Science and Ceramics, AGH – University of Science and Technology, al. Mickiewicza 30, 30-059 Cracow, Poland
[10] Department of Radiological Sciences, College of Applied Medical Sciences, Najran University, Najran 1988, Saudi Arabia.

* Author to whom correspondence should be addressed: bsoltan@kku.edu.sa (B. Sultan)

1. INTRODUCTION

The ongoing advancement of technologies utilizing ionizing radiation, spanning medical diagnostics and radiotherapy, nuclear power generation, aerospace exploration, and industrial radiography, has precipitated a critical and

© Ariston Publications 2025. All rights reserved.

persistent demand for effective, reliable, and adaptable radiation shielding materials [1-4]. Conventional shielding materials like lead and concrete, while effective, present significant drawbacks including toxicity, opacity, weight, and limited design flexibility for specialized applications. Consequently, the scientific community has intensified efforts to develop novel glass-based shields that offer a compelling combination of transparency, structural integrity, chemical durability, and tunable radiation attenuation properties. Within this pursuit, tellurite (TeO_2)-based glass systems have emerged as a particularly promising frontier due to their unique and advantageous physico-chemical characteristics [5-7].

Tellurite glasses possess an exceptional suite of properties that render them attractive for advanced optical and photonic applications, including a high refractive index, broad infrared transparency, low phonon energy, and significant nonlinear optical coefficients [8-11]. These attributes stem from the polarizable nature of the tellurium-oxygen network. However, a primary challenge in the utilization of pure TeO_2 is its relatively poor glass-forming ability and thermal stability, a consequence of its weak bond structure which makes the network inherently less compact [12, 13]. To overcome these limitations and tailor the material for specific functions, network intermediates and modifiers are systematically incorporated. The addition of boron oxide (B_2O_3), for instance, significantly enhances the glass-forming range, improves chemical durability, and stabilizes the melt, facilitating more robust fabrication [14]. Furthermore, the introduction of heavy metal oxides (HMOs) such as bismuth oxide (Bi_2O_3) serves a dual purpose: it dramatically increases the density of the glass, a parameter directly proportional to gamma-ray attenuation, while also modifying the optical and thermal expansion properties [15, 16]. The synergistic combination of TeO_2 and B_2O_3 within a borotellurite matrix promotes the formation of stronger covalent bonds and increases the concentration of bridging oxygen atoms, thereby enhancing the overall thermal stability and chemical resistance of the resulting glass [17-19].

In the specific context of radiation shielding, the incorporation of high-density, high-atomic-number constituents is paramount for efficient attenuation of high-energy photons via dominant interactions like the photoelectric effect and Compton scattering [20, 21]. This has logically directed research towards the integration of rare-earth oxides (REOs) into glass matrices. Rare-earth elements, typically possessing high atomic numbers (Z=57-71) and densities, are effective in increasing the overall effective atomic number (Z_{eff}) and electron density of the glass, thereby elevating the probability of photon interactions [22]. Previous studies have substantiated that tellurite glasses containing heavy oxides like Bi_2O_3 and PbO exhibit promising radiation shielding characteristics [23-26]. Moreover, research on borotellurite systems modified with TeO_2 and Bi_2O_3 has reported beneficial effects such as elevated glass transition temperatures, reduced optical band gaps, and improved resistance to devitrification, broadening their potential utility into areas like optical amplifiers, solid-state lasers, and sensing devices [27, 28].

The novelty of the present work lies in the systematic experimental investigation and comprehensive analysis of a multi-component glass system specifically designed for shielding efficacy, where the synergistic effects of titanium oxide (TiO_2) and bismuth oxide (Bi_2O_3) are combined with targeted rare-earth doping to optimize both structural stability and radiation attenuation. While individual impacts of some components have been studied, the specific composition $45TeO_2–25B_2O_3–20Bi_2O_3–7TiO_2–3RE$ (where RE = La, Ce, Sm, Er, Yb) represents a tailored approach to balance glass-forming ability (via B_2O_3), density enhancement (via Bi_2O_3 and REOs), and network stabilization (via TiO_2 and rare-earth ions) to create a superior shielding material. Building upon prior experimental work by our group which involved the preparation and preliminary gamma-ray spectroscopic analysis of these glasses using isotope sources (Am-241, Cs-137, Co-60) [29], this study delves deeper into a thorough theoretical evaluation of their shielding performance. Utilizing the established Phy-X/PSD software platform [30], we extend the analysis across a continuous, broad energy spectrum from 0.015 to 15 MeV. This approach allows for the detailed determination of critical shielding parameters, including the linear and mass attenuation coefficients (μ, μ/ρ), half-value layer (HVL), tenth-value layer (TVL), mean free path (MFP), effective atomic number (Z_{eff}), effective electron density (N_{eff}), equivalent atomic number (Z_{eq}), and atomic/electronic cross-sections (ACS, ECS). Additionally, recognizing the importance of mixed-field radiation environments, the fast neutron removal cross-section (Σ_R) is also calculated to preliminarily assess the capability of the material in moderating fast neutrons, which are often present alongside high-energy photon fluxes. This comprehensive multi-parameter assessment provides a robust and complete picture of the potential of these rare-earth-doped tellurite glasses for deployment in demanding radiation shielding applications.

2. EXPERIMENTAL DETAILS

2.1. Glass Synthesis, Density Measurement, and Physical Characterization

The foundation of this investigation lies in the experimental fabrication and primary characterization of a novel series of multi-component oxide glasses. Five distinct glass samples were synthesized based on the molar composition $45TeO_2–25B_2O_3–20Bi_2O_3–7TiO_2–3RE$, where the rare-earth oxide (RE) component was systematically varied to include La_2O_3, Ce_2O_3, Sm_2O_3, Er_2O_3, and Yb_2O_3. This parent series is designated as BBTTRE, with individual samples coded as BBTTLa, BBTTCe, BBTTSm, BBTTEr, and BBTTYb, corresponding to the incorporated rare-earth ion. The detailed molar compositions are cataloged in Table 1.

The glasses were prepared using the conventional melt-quenching technique, a method renowned for its reliability in producing homogeneous bulk glass samples.

© Ariston Publications 2025. All rights reserved.

Table 1. Elemental compositions and densities of the prepared glass.

Sample code	Glass composition (mol%)									Sample color	*P* (g/cm^3)
	TeO_2	B_2O_3	Bi_2O_3	TiO_2	La_2O_3	Ce_2O_3	Sm_2O_3	Er_2O_3	Yb_2O_3		
BBTTLa	45	25	20	7	3	—	—	—	—		5.67
BBTTCe	45	25	20	7	—	3	—	—	—		6.08
BBTTSm	45	25	20	7	—	—	3	—	—		6.17
BBTTEr	45	25	20	7	—	—	—	3	—		6.21
BBTTYb	45	25	20	7	—	—	—	—	3		6.31

High-purity (≥99.9%) precursor powders of tellurium(IV) oxide (TeO_2), boron oxide (B_2O_3), bismuth(III) oxide (Bi_2O_3), titanium(IV) oxide (TiO_2), and the respective rare-earth oxides were used as starting materials. For each composition, a batch corresponding to approximately 20 grams of final product was meticulously weighed using a high-precision analytical balance. The mixed powders were then subjected to thorough grinding in an agate mortar to ensure a homogeneous mixture at the particulate level, a critical step for achieving chemical uniformity in the final glass.

The homogenized batches were transferred to high-purity alumina (Al_2O_3) crucibles and introduced into a programmable electric furnace. The melting protocol involved a controlled heating regime. The temperature was gradually raised to 900°C at a rate of 10°C per minute and held at this temperature for 60 minutes to allow for complete decomposition of carbonates, elimination of volatile constituents, and initial reaction between the oxides. Subsequently, the temperature was increased to the final melting temperature of 1100°C, which was maintained for a period of 90 minutes. During this stage, the melt was periodically stirred using a fused quartz rod to promote homogeneity and eliminate air bubbles. The molten glass was then rapidly quenched by pouring it onto a pre-heated stainless-steel mold and immediately pressed with another steel plate to form discs of approximately 2-3 mm thickness. This rapid quenching process is essential to bypass crystallization and freeze the disordered glassy network. To relieve internal thermal stresses, the as-cast glasses were immediately transferred to an annealing furnace held at a temperature of 350°C, which is below their glass transition temperature (T_g). They were annealed at this temperature for 3 hours before being allowed to cool slowly to room temperature inside the switched-off furnace. The resulting glass samples were then ground and polished to obtain parallel faces with optical quality, a prerequisite for accurate density, optical, and radiation attenuation measurements.

The physical density (ρ) of each polished glass sample, a fundamental property directly influencing its shielding efficacy, was determined at room temperature using the Archimedes principle with distilled water (ρ_{water} = 0.998 g/cm³ at 20°C) as the buoyant liquid. The measurement was performed using a high-precision microbalance capable of resolving 0.1 mg. Each sample was weighed in air (W_{air}) and subsequently when immersed in distilled water (W_{water}). The density was calculated using the standard formula: $\rho_{glass} = [W_{air} / (W_{air} - W_{water})] * \rho_{water}$. This procedure was repeated five times for each sample, and the reported density values in Table 1 represent the mean, with an associated experimental uncertainty of ±0.001 g/cm³. A clear trend of increasing density is observed with the progression from La to Yb, correlating with the increasing atomic mass of the rare-earth cation, culminating in the highest density of 6.31 g/cm³ for the ytterbium-doped BBTTYb glass. The visual appearance and color of the samples, also noted in Table 1, arise from electronic transitions associated with the specific rare-earth ions and the overall glass matrix. The comprehensive data on other physical parameters, such as molar volume, oxygen packing density and detailed optical properties, including photoluminescence spectra, refractive index, and optical band gap determined from UV-Vis-NIR spectroscopy, have been reported and discussed in detail in our previous publication [20]. That prior work established that the BBTTYb sample also possessed the highest optical energy gap and average stretching force constant, indicating a more robust and tightly cross-linked network structure.

2.2. Theoretical Framework for Attenuation Parameter Analysis

In order to evaluate a novel compound to be used in ionizing radiation shielding, an investigation of several physical parameters is required. The linear attenuation coefficient (μ) is one of the most important variables. This quantity determines the probability of a material attenuating the primary photons through absorption and scattering interactions per unit path length. The three most common interactions are; photoelectric effects, Compton scattering, and pair production. The following is the equation used to determine, μ, [22]:

$$\mu = \frac{1}{L} ln \frac{I_t}{I_0} \quad (1)$$

© Ariston Publications 2025. All rights reserved.

where L is the thickness of the sample, I_t represents the intensity of transmitted photons and I_0 denotes the intensity of the initial photons. Resulted μ is measured in cm^{-1} unit and it is dependent on density. Therefore, the mass attenuation coefficient (μ_m) is the related attenuation coefficient that describes the attenuation characteristics in the absorber based on density. μ_m is calculated as the μ divided by the density of the absorber and given in units of (cm^2/g) as in the following equation [23]:

$$\mu_m = \sum_n w_n \left[\frac{\mathrm{LAC}}{\rho}\right]_n \quad (2)$$

where w_n refers to the total weight of the compound's individual fractions and n is the total mass of the element. There are three special quantities that typically describe the absorber thickness properties for a monoenergetic narrow photon beam. The half value layer (HVL), mean free path (MFP), and tenth value layer (TVL) is these parameters. The definition of HVL, also known as $(X_{\frac{1}{2}})$, is the thickness of a homogeneous absorber required to decrease a photon beam's intensity in half from its initial value. The relationship between the LAC and HVL is determined from the basic definition of both quantities using the following equation [23]:

$$HVL = \frac{ln2}{\mu} \quad (3)$$

The second parameter MFP represents the average distance traveled by a photon without undergoing any interaction in the absorber. MFP can be calculated from the following equation [23]:

$$MFP = \frac{1}{\mu} \quad (4)$$

The thickness of a homogeneous material that reduces the photon beam's intensity to a tenth of its original intensity is referred to as TVL is determined using the following equation [23]:

$$TVL = \frac{ln10}{\mu} \quad (5)$$

Atomic and electronic cross-sections (σ_a and σ_e) are defined as the probability that absorber atoms or electrons, with a given ionization level or excitation state, will interact with an incident photon. σ_a and σ_e are estimated to quantify the probability of a specified particle-particle interaction. Both quantities are given in (cm^2/g) and equations 6 and 7 mathematically express by the following [24]:

$$\sigma_a = \frac{1}{N_A}\sum_i f_i A_i \left(\frac{\mu}{\rho}\right)_i \quad (6)$$

$$\sigma_e = \frac{1}{N_A}\sum_j f_j \frac{A_j}{Z_j}\left(\frac{\mu}{\rho}\right)_j \quad (7)$$

Where f_i is fraction by mole of the ith atomic element, A_i is atomic weight of the ith atomic element, Z_j is atomic number and N_A is Avogadro constant. The probability of photon interaction increases when increasing the effective atomic number (Z_{eff}) and effective electron density (N_{eff}). These vital quantities are important in radiation shielding in order to evaluate the material effectiveness for photon beam attenuation, absorption, and scattering interactions. Therefore, significant consideration is given to enhancing the shielding characteristics of a specific complex material. The Z_{eff} and N_{eff} can be calculated from the following equations [24]:

$$Z_{eff} = \frac{\sigma_a}{\sigma_e} \quad (8)$$

$$N_{eff} = \frac{N_A}{\sum_i f_n A_n} Z_{eff} \sum \beta_n = \frac{\mu_m}{\sigma_e} \quad (9)$$

where $\sum \beta_n$ refers to the shielding material's total number of component elements. The other terms are defined in previous equations. Based on each corresponding composite element, a shielding compound is selected using the equivalent atomic number (Z_{eq}). The parameter Z_{eq} can be calculated using the following equation [25, 26]:

$$Z_{eq} = \frac{Z_1(logR_2 - logR) + Z_2(logR - logR_1)}{(logR_2 - logR_1)} \quad (10)$$

Where Z_1 and Z_2 are the atomic numbers for each element, R_1 and R_2 hold for the ratios of the shielding medium's mass attenuation coefficient to that of the shielding medium. Estimation of the exposure buildup factor (EBF) is of a great importance to determine the thickness of the shielding material under investigation. EBF is determined by dividing the whole exposure by the exposure of the primary beam that passes through the shielding material without interacting. The exposure geometric progression (G-P) fitting parameters to the corresponding EBF have been calculated in a similar procedure as Z_{eq} using the following formula [27]:

$$G = \frac{g_1(logZ_2 - logZ_{eff}) + g_2(logZ_{eff} - logZ_1)}{(logZ_2 - logZ_1)} \quad (11)$$

where g_1 and g_2 are the G-P fitting function parameters produced from ANSI/ANS for the elements with atomic numbers Z_1 and Z_2.For all constructed compounds, after interpolating the required parameters, the following formula may be used to estimate EBF [28].

$$B(E,x) = 1 + \frac{(bC-1)}{(K-1)}(K^x - 1), K \neq 1 \quad (12)$$

$$B(E,x) = 1 + (b-1)x, K \neq 1 \quad (13)$$

$$K(E,x) = cx^a + d\frac{tanh\left(\frac{x}{X_k} - 2\right) - tanh(-2)}{1 - tanh(-2)}, x \leq 40mfp \quad (14)$$

where E is the specific photon energy in MeV, $\boldsymbol{x}$ is the source-

© Ariston Publications 2025. All rights reserved.

detector distance measured in unit of MFP, a, b, c, d, and X_k, refer to the G-P fitting parameters while *K(E,x)* denotes the photon dose multiplicative factor and variation in shape of the energy spectrum. To determine the ability of specific shielding materials to harden neutrons, the fast neutron-removal cross-section (FNRCS) is calculated with the following equation [29]:

$$\Sigma_R = \Sigma_i \rho_i (\Sigma_R/\rho) \quad (15)$$

where ρi and (ΣR/ρ)i represent the partial density.

3. RESULTS AND DISCUSSION

3.1. Structural and Optical Properties

A comprehensive analysis of the structural, physical, and optical characteristics of the prepared BBTTRE glass series ($45TeO_2$–$25B_2O_3$–$20Bi_2O_3$–$7TiO_2$–3RE) has been detailed in a prior publication by our research group [20]. Those findings established a critical foundation for interpreting the radiation shielding performance elucidated in the present work. Notably, a consistent trend was observed where the replacement of the rare-earth ion from La^{3+} to Yb^{3+} induced significant modifications in the glass network. The ytterbium-doped sample, BBTTYb, exhibited the most robust structural profile, characterized by the highest optical energy band gap (2.8 eV), the greatest number of bonds per unit volume (7.14×10^{22} cm^{-3}), and the highest average stretching force constant (303.04 Nm^{-1}) [20]. These parameters collectively indicate a more polymerized, rigid, and chemically durable glass network for the BBTTYb composition. The increased bond strength and network connectivity are directly correlated with the higher measured density and are anticipated to influence the interaction of material with ionizing radiation, particularly in enhancing photon absorption probabilities.

3.2. Gamma-Ray Shielding Performance

3.2.1. Attenuation Coefficients

The fundamental parameters defining a material's capacity to attenuate gamma radiation are the linear attenuation coefficient (μ) and the mass attenuation coefficient (μ/ρ). Figure 1(a) presents the variation of the linear attenuation coefficient (μ) with photon energy across the expansive range of 0.015 to 15 MeV for all five BBTTRE glasses. The observed trend is archetypal of heavy-element-containing materials and is governed by the dominant photon interaction mechanisms operative at different energy regimes. At the lowest energies (0.015 – 0.1 MeV), the coefficients are exceptionally high, exhibiting a sharp decrease with increasing energy. This region is dominated by the photoelectric effect, where the cross-section is proportional to approximately Z^4/E^3, making it extremely sensitive to atomic number and energy. The distinct discontinuities visible as sharp drops in the curve, specifically around 0.1 MeV, correspond to the K-absorption edges of the high-Z constituents in the glass, such as bismuth (K-edge at 90.5 keV) and tellurium (K-edge at 31.8 keV). As energy increases beyond approximately 0.1 MeV, the Compton scattering process becomes predominant. In this region (0.1 – 5 MeV), the attenuation coefficient decreases gradually and exhibits a near-linear dependence on energy on the logarithmic plot, which is characteristic of Compton scattering where the cross-section per electron is roughly constant. Above the threshold of 1.022 MeV, the pair production interaction begins to contribute, leading to a gradual increase in the μ values for energies above 3-4 MeV, as seen in the upward curvature of the plots.

While Figure 1(a) demonstrates the absolute stopping power per centimeter, Figure 1(b) displays the mass attenuation coefficient (μ/ρ), which normalizes the attenuation to the material's density, allowing for a more fundamental comparison of the interaction probabilities. All samples follow an identical energy-dependent trend for the reasons described. The critical insight from Figure 1(b) is revealed in the magnified inset focusing on the high-energy region (4-15 MeV). Here, a clear ranking emerges directly correlated with the sample density. The BBTTLa glass, with the lowest density (5.67 g/cm^3), possesses the lowest μ/ρ values. A systematic increase is observed through BBTTCe (6.08 g/cm^3), BBTTSm (6.17 g/cm^3), and BBTTEr (6.21 g/cm^3), culminating with BBTTYb (6.31 g/cm^3) exhibiting the highest mass attenuation coefficients. This is a significant finding because, in the pair production region, the cross-section has a Z^2 dependence. The progressive increase in density from La to Yb is intrinsically linked to the incorporation of heavier rare-earth cations with higher atomic numbers, which enhances the overall effective atomic number (Z_{eff}) of the composite glass. Consequently, the BBTTYb sample, with its maximized density and Z_{eff}, offers the highest probability for photon interactions per unit mass at high energies, underscoring its superior intrinsic shielding capability.

3.2.2. Atomic and Electronic Cross-Sections

To delve deeper into the interaction mechanics at the atomic level, the atomic cross-section (ACS, σ_e) and electronic cross-section (ECS, σ_e) were evaluated. Figure 2(a) plots the ACS, which represents the probability of interaction per atom. At very low energies, the ACS values are extraordinarily high due to the overwhelming dominance of the photoelectric effect, which is an atomic process. As energy increases into the Compton scattering regime, the ACS drops sharply because Compton scattering is primarily an interaction with loosely bound or free electrons, and its cross-section per atom is lower than that of the photoelectric effect in this energy range. The subsequent gentle rise at very high energies is again attributable to the onset of pair production.

© Ariston Publications 2025. All rights reserved.

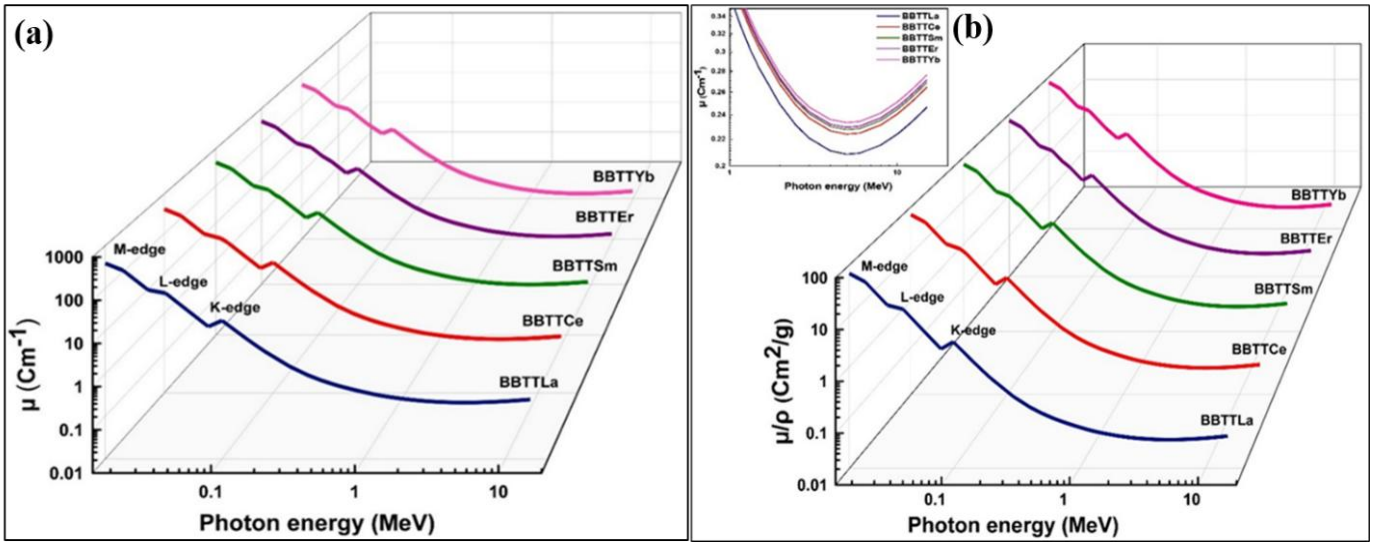

Fig. 1. Shielding parameters: (a) Linear attenuation coefficient (b) mass attenuation coefficient in relation to photon energies in the range between 0.015 and 15 MeV.

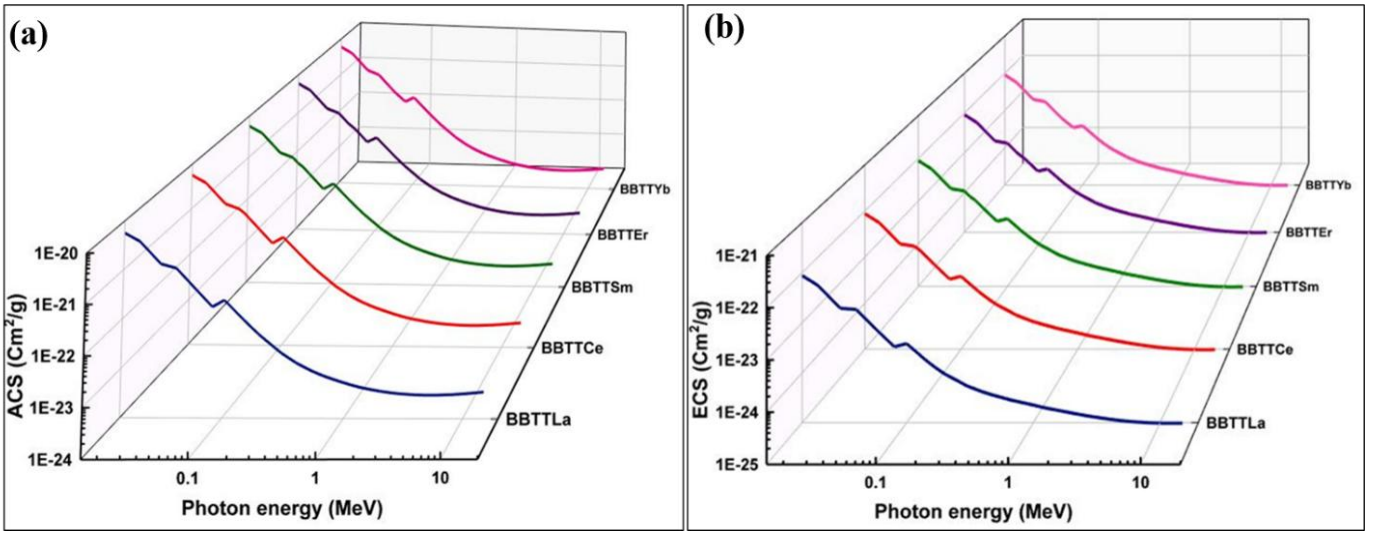

Fig. 2. Resulted simulation of the (a) Calculated ACS for all glass samples doped with different rare earth elements at various energy ranges; (b) ECS values as a function of photon energy for all glass compositions.

Figure 2(b) presents the ECS, the interaction probability per electron. The ECS profile mirrors that of the ACS at lower energies because photoelectric absorption also results in the ejection of an electron. However, the behavior in the Compton region is different. Since Compton scattering is an electron-dependent interaction, the ECS shows a less dramatic decline compared to the ACS in the mid-energy range and provides a clearer signature of the scattering process. The parallel behavior of all samples in both figures confirms that the fundamental interaction physics is consistent across the series; the differences in magnitude, particularly at high energies, are again dictated by the composite atomic number and density differences between the glasses.

3.2.3. Half-Value Layer, Tenth-Value Layer, and Mean Free Path

For practical shielding design, engineers require parameters that directly translate to required material thickness. The Half-Value Layer (HVL) and Tenth-Value Layer (TVL) are precisely such metrics, defining the thickness needed to reduce radiation intensity by 50% and 90%, respectively. Figure 3(a) displays the HVL as a function of energy. The graph inversely mirrors the μ plot: where attenuation is high

© Ariston Publications 2025. All rights reserved.

(low energy), the HVL is very small (a few millimeters or less), indicating that only a thin slice of glass is needed for effective shielding. As the attenuation coefficient decreases in the Compton region, the HVL increases substantially, reaching several centimeters at MeV energies. Figure 3(b) presents the TVL, which follows a similar trend but with greater absolute thickness values, as expected since TVL ≈ 3.32 × HVL. These figures critically show that a 10 cm thickness of any BBTTRE glass provides exceptional attenuation (TVL-level or better) for photons below 100 keV, and still offers significant reduction (exceeding a factor of 10) for higher energies up to several MeV.

The Mean Free Path (MFP), plotted in Figure 3(c), is the average distance a photon travels between successive interactions. It is the inverse of the linear attenuation coefficient (MFP = 1/μ). Its trend is identical to HVL, with very short paths at low energy and longer paths at high energy. The subtle but important differentiation between samples is most visible in the high-energy portion of the MFP plot. BBTTLa, with the lowest density, has the longest MFP, meaning photons penetrate further on average before interacting. In contrast, BBTTYb consistently shows the shortest MFP across the entire spectrum, most notably above 1 MeV. This quantitatively confirms that the Yb-doped glass is the most effective shield, as incident photons undergo interactions more frequently within a given thickness.

A pivotal comparative analysis is shown in Figure 3(d), where the HVL of the BBTTRE glasses is plotted against commercially available and widely used radiation shielding glasses: RS-253-G18, RS-360, and RS-520 [30]. This comparison places the experimental glasses in a real-world context. The plot reveals that the BBTTYb glass performs comparably to these industrial standards across a broad energy range. Remarkably, in the critical diagnostic and mid-energy range (from around 0.1 to 1 MeV), BBTTYb exhibits a lower HVL than RS-253-G18 and is competitive with RS-360. This demonstrates that the novel BBTTYb composition is not merely an academic curiosity but a viable candidate with performance metrics that match or exceed those of established commercial products designed specifically for radiation protection.

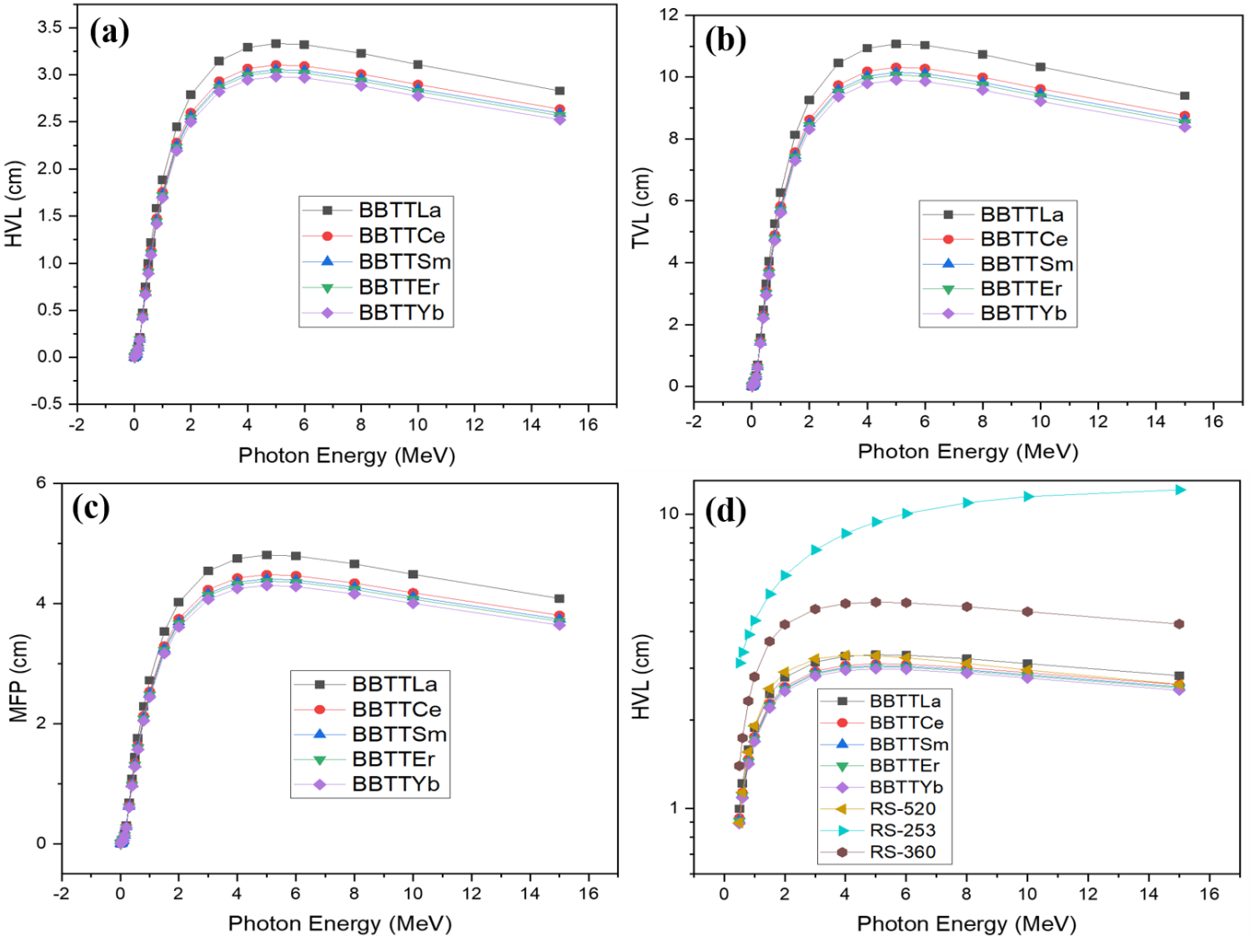

Fig. 3. Resulted simulation of the (a) HVL; (b) TVL; (c) MFP values of the investigated glasses with different standard materials in the range of 0.015-15 MeV.

© Ariston Publications 2025. All rights reserved.

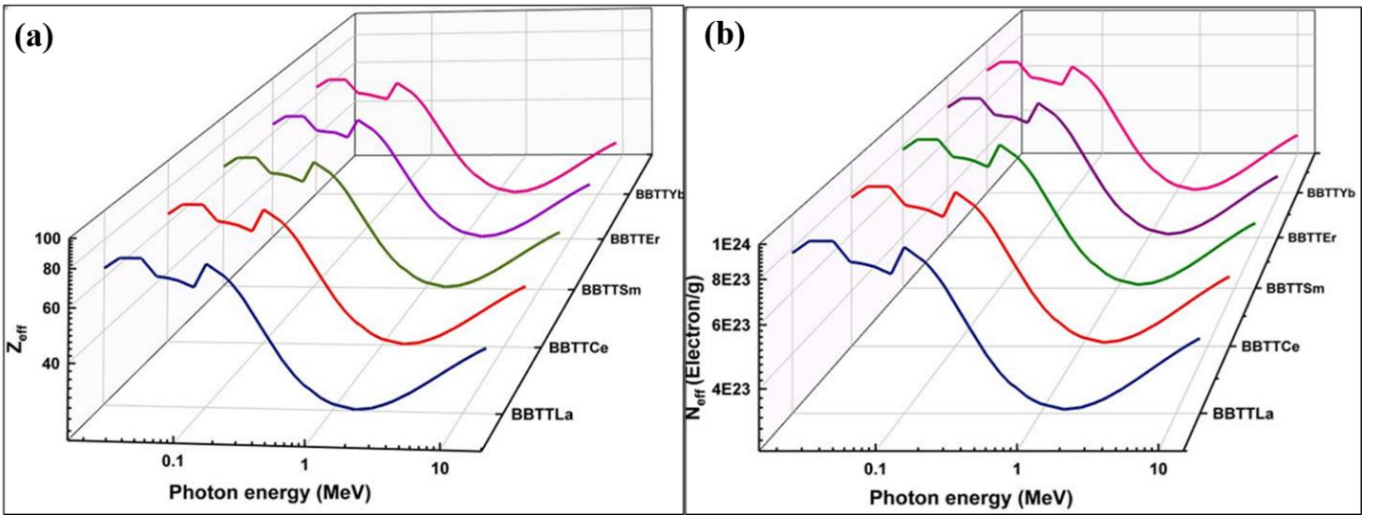

Fig. 4. (a) Studied Z_{eff} against photon energy for all the glass samples. K-absorption edge is shown at 0.1 MeV and (b) Resulted N_{eff} of all BBTT samples at various photon energies.

3.2.4. Effective Atomic Number and Effective Electron Density

The Effective Atomic Number (Z_{eff}) is a vital parameter that condenses the complex composition of a multi-element material into a single number equivalent to the atomic number of a hypothetical element that would attenuate photons identically. Figure 4(a) charts Z_{eff} against photon energy. The plot exhibits a characteristic energy dependence linked to the dominant interaction mechanism [31, 32]. At very low energies (≤0.1 MeV), Z_{eff} is high because the photoelectric effect, with its ~Z^4 dependence, gives disproportionate weight to the highest-Z elements (like Bi). The sharp peak and subsequent drop near 0.1 MeV correspond to the K-edge, beyond which the photoelectric cross-section decreases rapidly. In the Compton scattering-dominated region (~0.3 – 5 MeV), Z_{eff} reaches a minimum and plateaus. Compton scattering cross-section per electron is largely independent of Z, so Z_{eff} in this region reflects a weighted average of the atomic numbers, weighted by the electron fraction. As pair production becomes significant above 5 MeV, Z_{eff} increases again because the pair production cross-section varies approximately with Z^2. Throughout this progression, BBTTYb maintains the highest Z_{eff} values, followed by BBTTEr, BBTTSm, BBTTCe, and BBTTLa. This hierarchical order perfectly aligns with the increasing atomic number of the dopant rare-earth ion (Yb=70, Er=68, Sm=62, Ce=58, La=57) and the resulting density trend, providing a fundamental atomic-scale explanation for the observed macroscopic shielding superiority of BBTTYb.

Closely related to Z_{eff} is the Effective Electron Density (N_{eff}), shown in Figure 4(b). N_{eff} represents the number of electrons per gram available for interactions. Its energy dependence closely mirrors that of Z_{eff} for a fundamental reason: $N_{eff} = (\mu/\rho) / \sigma_e$, and since σ_e is directly involved in the calculation of Z_{eff}, the two parameters are intrinsically linked. The trends are consistent, with BBTTYb exhibiting the highest N_{eff} values. A material with higher N_{eff} possesses a greater density of electronic targets for Compton scattering, further contributing to its attenuation efficacy in the mid-energy range.

3.2.5. Effective Conductivity and Scattering Ratio

The Effective Conductivity (C_{eff}), derived from N_{eff}, is an indicator of the material's electronic response under photon irradiation. Figure 5(a) displays C_{eff} as a function of energy. The profile is reminiscent of the Z_{eff} and N_{eff} curves. The high values at low energies correspond to the high probability of photoelectric absorption, which liberates electrons and thus momentarily increases local conductivity. The minimum observed around 1-3 MeV coincides with the Compton minimum region, where the interaction probability per electron is at its lowest. The subsequent rise at very high energies is attributed to pair production, which generates two charged particles (an electron and a positron) per event, thereby enhancing conductivity. This parameter, while not a direct shielding metric, offers insight into the potential for radiation-induced electrical effects within the material.

Figure 5(b) presents the ratio (R) of the incoherent (Compton) scattering cross-section to the total attenuation cross-section. This ratio is profoundly important for understanding secondary radiation effects. A high R value indicates that Compton scattering is the primary interaction, which generates scattered photons that can contribute to dose buildup beyond the shield. In the very low-energy photoelectric region, R is nearly zero because absorption is total. As energy increases past the K-edge, R rises sharply to a broad maximum between 0.5 and 5 MeV, confirming that Compton scattering is the overwhelmingly dominant process in this crucial energy band.

© Ariston Publications 2025. All rights reserved.

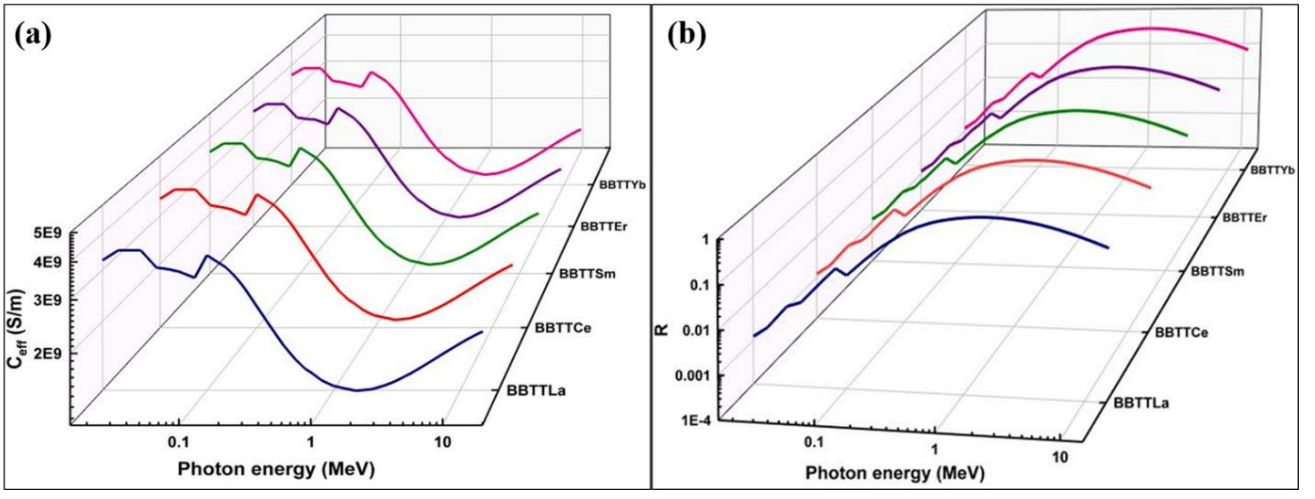

Fig. 5. (a) Plot of Ceff values against incident photon energy for the prepared BBTT samples, and (b) Simulated R values for tested BBTT glass samples at different energy ranges.

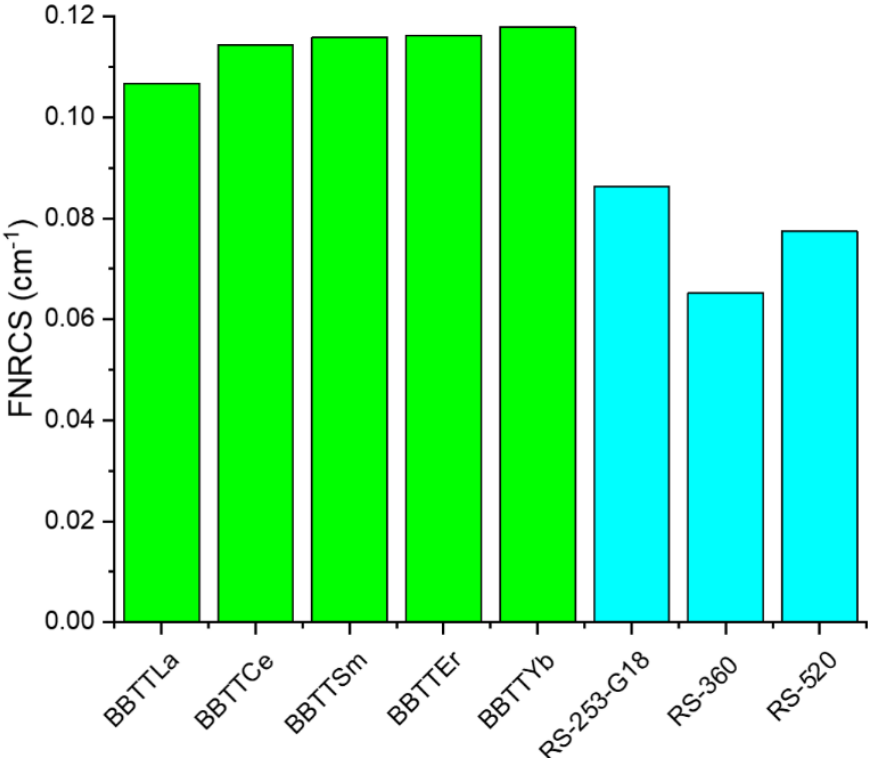

Fig. 6. Bar chart representing the calculated fast neutron-removal cross-sections for the prepared glasses (TBTL) and for other available glass shielding materials.

This highlights the necessity of considering buildup factors in shield design for these energies. At energies above 10 MeV, the R ratio declines as pair production, an absorption process, begins to claim a larger share of the total interaction probability.

3.2.6. Fast Neutron Removal Cross-Section

In applications involving high-energy photon beams, such as radiotherapy linear accelerators above 10 MeV, photoneutron production becomes a significant concern. Therefore, a complete shielding material should also possess some capability to moderate these fast neutrons. Figure 6 presents a bar chart comparing the Fast Neutron Removal Cross-Section (Σ_R) for the BBTTRE glasses with the same commercial standards. The removal cross-section represents the probability per unit path length that a fast neutron will be removed from the beam through scattering reactions that lower its energy. Higher Σ_R values indicate better neutron

© Ariston Publications 2025. All rights reserved.

shielding potential. The results show that the Σ_R values for the BBTTRE glasses range from approximately 0.065 to 0.118 cm^{-1}. Notably, BBTTYb achieves the highest Σ_R among the prepared samples. While these values are generally lower than those of the dedicated commercial shielding glasses (RS-360, RS-520), they are comparable to or exceed that of RS-253-G18. This indicates that the BBTTRE glasses, particularly BBTTYb, possess a non-negligible inherent capacity for fast neutron moderation due to the presence of light elements like boron (B_2O_3) and oxygen in the matrix. Boron-10 is especially effective for thermal neutron capture, though the removal cross-section primarily addresses fast neutrons. This dual-functionality, competent gamma attenuation coupled with measurable neutron removal, enhances the utility of these materials for mixed-field radiation environments encountered in advanced medical and nuclear applications.

4. CONCLUSION

This experimental study successfully synthesized and characterized a series of rare earth-doped tellurite glasses with the composition $45TeO_2$–$25B_2O_3$–$20Bi_2O_3$–$7TiO_2$–3RE (RE = La, Ce, Sm, Er, Yb) for radiation shielding applications. The glasses were fabricated using a conventional melt-quenching technique, and their attenuation properties were experimentally evaluated using gamma-ray sources, with supplementary theoretical analysis performed via the Phy-X/PSD platform. The results clearly indicate that the incorporation of rare earth oxides significantly enhances the radiation shielding performance of the base glass matrix. Among the tested compositions, the Yb_2O_3-doped sample (BBTTYb) exhibited the most promising characteristics, including the highest density (6.31 g/cm^3), the lowest half-value layer, and the smallest mean free path across the investigated energy range. This superior performance is ascribed to the combined effect of increased density, elevated effective atomic number, and improved structural compactness due to ytterbium inclusion. All glass samples demonstrated effective attenuation, particularly at lower gamma-ray energies where the photoelectric effect dominates, while also maintaining appreciable shielding at higher energies relevant to medical and industrial applications. Comparative analysis with commercial shielding glasses confirms the competitive performance of these materials. Furthermore, the assessed fast neutron removal cross-section suggests additional utility in environments with mixed neutron-gamma fields. The correlation between experimental measurements and theoretical simulations validates the reliability of the data and underscores the role of rare earth ions in tailoring shielding properties. In conclusion, this work provides experimental evidence that rare earth-doped tellurite glasses, especially those containing Yb_2O_3, are highly effective radiation shielding materials. Their favorable optical, thermal, and mechanical properties, coupled with tunable attenuation performance, make them suitable candidates for deployment in radiotherapy suites, nuclear installations, diagnostic imaging centers, and aerospace applications. Future research will focus on scaling production and testing under real-field conditions.

DECLARATIONS

Ethical Approval

We affirm that this manuscript is an original work, has not been previously published, and is not currently under consideration for publication in any other journal or conference proceedings. All authors have reviewed and approved the manuscript, and the order of authorship has been mutually agreed upon.

Funding

Not applicable

Availability of data and material

All of the data obtained or analyzed during this study is included in the report that was submitted.

Conflicts of Interest

The authors declare that they have no financial or personal interests that could have influenced the research and findings presented in this paper. The authors alone are responsible for the content and writing of this article.

Authors contributions

All authors contributed equally in the preparation of this manuscript.

REFERENCES

[1] Wang, J.S., Vogel, E.M. and Snitzer, E., **1994**. Tellurite glass: a new candidate for fiber devices. *Optical Materials*, 3(3), pp.187-203.

[2] Jaba, N., Kanoun, A., Mejri, H., Selmi, A., Alaya, S. and Maaref, H., **2000**. Infrared to visible up-conversion study for erbium-doped zinc tellurite glasses. *Journal of Physics: Condensed Matter*, 12(20), pp.4523-4534.

[3] Yousef, E., Hotzel, M. and Rüssel, C., **2007**. Effect of ZnO and Bi_2O_3 addition on linear and non-linear optical properties of tellurite glasses. *Journal of Non-Crystalline Solids*, 353(4), pp.333-338.

[4] Damak, K., Yousef, E.S., Al-Shihri, A.S., Seo, H.J., Rüssel, C. and Maâlej, R., **2014**. Quantifying Raman

© Ariston Publications 2025. All rights reserved.

and emission gain coefficients of Ho^{3+} doped $TeO_2 \cdot ZnO \cdot PbO \cdot PbF_2 \cdot Na_2O$ (TZPPN) tellurite glass. *Solid State Sciences*, 28, pp.74-80.

[5] Bale, S., Rahman, S., Awasthi, A.M. and Sathe, V., **2008**. Role of Bi_2O_3 content on physical, optical and vibrational studies in Bi_2O_3–ZnO–B_2O_3 glasses. *Journal of Alloys and Compounds*, 460(1), pp.699-703.

[6] Jan, N., Sahar, M.R., Ghoshal, S., Ariffin, R., Md Supar, R. and Hamzah, K., **2014**. Absorption Spectra of Neodymium Doped Tellurite Glass. *Advanced Materials Research*, 895, pp.395-399.

[7] Elkhoshkhany, N., Abbas, R., El-Mallawany, R. and Hathot, R., **2017**. Optical properties and crystallization of bismuth boro-tellurite glasses. *Journal of Non-Crystalline Solids*, 476, pp.15–24.

[8] Boda, R., Shareefuddin, M.D., Chary, M.N. and Sayanna, R., **2016**. FTIR and optical properties of europium doped lithium zinc bismuth borate glasses. *Materials Today: Proceedings*, 3(6), pp.1914–1922.

[9] Gupta, N., Kaur, A., Khanna, A., Gonzàlez, F., Pesquera, C., Iordanova, R. and Chen, B., **2017**. Structure-property correlations in TiO_2-Bi_2O_3-B_2O_3-TeO_2 glasses. *Journal of Non-Crystalline Solids*, 470, pp.168–177.

[10] Sapian, I.N., Yusof, M.I.M. and Yahya, A.K., **2014**. Elastic and Structural Properties of (95-x) TeO_2-$5La_2O_3$-xTiO_2 Lanthanum Tellurite Glass System. *Chalcogenide Letters*, 11(9), pp.471–484.

[11] Maheshvaran, K., Linganna, K. and Marimuthu, K., **2011**. Composition dependent structural and optical properties of Sm^{3+} doped boro-tellurite glasses. *Journal of Luminescence*, 131(12), pp.2746–2753.

[12] Gaikwad, D.K., Sayyed, M.I., Obaid, S.S., Issa, S.A.M. and Pawar, P.P., **2018**. Gamma ray shielding properties of TeO_2-ZnF_2-As_2O_3-Sm_2O_3 glasses. *Journal of Alloys and Compounds*, 765, pp.451–458.

[13] Singh, G.P., Kaur, P., Kaur, S. and Singh, D.P., **2012**. Investigation of structural, physical and optical properties of CeO_2–Bi_2O_3– B_2O_3 glasses. *Physica B: Condensed Matter*, 407(21), pp.4168–4172.

[14] Sayyed, M.I., Laariedh, F., Kumr, A. and Al-Buriahi, M.S., **2020**. Experimental studies on the gamma photons-shielding competence of TeO_2–PbO–BaO–Na_2O–B_2O_3 glasses. *Applied Physics A*, 126(4), p.268.

[15] Kamislioglu, M., Guclu, E.A. and Tekin, H.O., **2020**. Comparative evaluation of nuclear radiation shielding properties of xTeO_2 + (100-x)Li_2O glass system. *Applied Physics A*, 126(1), p.55.

[16] Rammah, Y.S., Kavaz, E., Perişanoğlu, U., Kilic, G., El-Agawany, F.I. and Tekin, H.O., **2020**. Charged particles and gamma-ray shielding features of oxyfluoride semiconducting glasses: TeO_2-Ta_2O_5-ZnO/ZnF_2. *Ceramics International*, 46(16), pp.25035–25042.

[17] Lakshminarayana, G., Kaky, K.M., Baki, S.O., Ye, S., Lira, A., Kityk, I.V. and Mahdi, M.A., **2016**. Concentration dependent structural, thermal, and optical features of Pr^{3+}-doped multicomponent tellurite glasses. *Journal of Alloys and Compounds*, 686, pp.769–784.

[18] Gerward, L., Guilbert, N., Jensen, K.B. and Levring, H., **2004**. WinXCom—a program for calculating X-ray attenuation coefficients. *Radiation Physics and Chemistry*, 71(3-4), pp.653–654.

[19] Hussein, K.I., Alqahtani, M.S., Algarni, H., Zahran, H., Yaha, I.S., Grelowska, I., Reben, M. and Yousef, E.S., **2021**. MIKE: A new computational tool for investigating radiation, optical and physical properties of prototyped shielding materials. *Journal of Instrumentation*, 16, p.T07004.

[20] Elkhoshkhany, N., Marzouk, S., El-Sherbiny, M., Ibrahim, H., Burtan-Gwizdala, B., Alqahtani, M.S., Hussien, K.I., Reben, M. and Yousef, E.S., 2022. Investigation of structural, physical, and attenuation parameters of glass: TeO2-Bi2O3-B2O3-TiO2-RE2O3 (RE: La, Ce, Sm, Er, and Yb), and applications thereof. *Materials*, *15*(15), p.5393.

[21] Şakar, E., Özpolat, Ö.F., Alım, B., Sayyed, M.I. and Kurudirek, M., **2020**. Phy-X/PSD: development of a user friendly online software for calculation of parameters relevant to radiation shielding and dosimetry. *Radiation Physics and Chemistry*, 166, p.108496.

[22] Hubbell, J.H., **1999**. Review of photon interaction cross section data in the medical and biological context. *Physics in Medicine & Biology*, 44(1), pp.R1-R22.

[23] Tekin, H., Kavaz, E., Papachristodoulou, A., Kamislioglu, M., Agar, O. and Altunsoy Guclu, E., **2019**. Characterization of SiO_2–PbO–CdO–Ga_2O_3 glasses for comprehensive nuclear shielding performance: Alpha, proton, gamma, neutron radiation. *Ceramics International*, 45(15), pp.19206-19222.

 © Ariston Publications 2025. All rights reserved.

[24] Komatsu, T. and Dimitrov, V., **2019**. Features of electronic polarizability and approach to unique properties in tellurite glasses. *International Journal of Applied Glass Science*, 11(2), pp.253-271.

[25] Saudi, H.A., Gomaa, H.M., Sayyed, M.I. and Shaaban, K.S., **2019**. Investigation of bismuth silicate glass system modified by vanadium and copper cations for structural and gamma-ray shielding properties. *SN Applied Sciences*, 1(3), p.218.

[26] [26] Al-Hadeethi, Y., Sayyed, M.I., Mohammed, H. and Rimondin, L., **2020**. X-ray photons attenuation characteristics for two tellurite-based glass systems at dental diagnostic energies. *Ceramics International*, 46(2), pp.251–257.

[27] Harima, Y., Kurosawa, N. and Sakamoto, Y., **2014**. Parameter search of geometric-progression formula for gamma-ray isotropic point source buildup factors up to depths of 100 mfp, including contribution of secondary radiations. *Progress in Nuclear Science and Technology*, 4, pp.548-552.

[28] Almatari, M., Agar, O., Altunsoy, E.E., Kilicoglu, O., Sayyed, M.I. and Tekin, H.O., **2019**. Photon and neutron shielding characteristics of samarium doped lead alumino borate glasses containing barium, lithium and zinc oxides determined at medical diagnostic energies. *Results in Physics*, 12, pp.2123–2128.

[29] Chilton, A.B., Shultis, J.K. and Faw, R.E., **1984**. *Principles of Radiation Shielding*. 1st ed. New Jersey: Prentice Hall.

[30] Kurtulus, R., 2024. Recent developments in radiation shielding glass studies: a mini-review on various glass types. *Radiation Physics and Chemistry*, *220*, p.111701.

[31] Agar, O., Khattari, Z.Y., Sayyed, M.I., Tekin, H.O., Al-Omari, S., Maghrabi, M. and Zaid, M.H.M., **2019**. Evaluation of the shielding parameters of alkaline earth based phosphate glasses using MCNPX code. *Results in Physics*, 12, pp.101-106.

[32] Al-Hadeethi, Y. and Sayyed, M.I., **2020**. X-ray attenuation features of some tellurite glasses evaluated at medical diagnostic energies. *Applied Mathematics and Computation*, *365*, p.124712.

© Ariston Publications 2025. All rights reserved.